AGU PUBLICATIONS

JGR

Journal of Geophysical Research: Oceans

RESEARCH ARTICLE

10.1002/2014JC010210

Structure of the turbidity field in the Guadalquivir estuary: Analysis of observations and a box model approach

M. Díez-Minguito[1], A. Baquerizo[1], H. E. de Swart[2], and M. A. Losada[1]

[1]Environmental Fluid Dynamics Group, Andalusian Institute for Earth System Research, University of Granada, Granada, Spain, [2]Institute for Marine and Atmospheric Research Utrecht, Utrecht University, Utrecht, Netherlands

Key Points:
- Transport due to M4 and M2 current-SPM interaction controls the setting of ETM
- Mean advection, current-SPM covariance, and Stokes transport are the main drivers
- The semianalytical box model permits an evaluation of the morphodynamic balance

Correspondence to:
M. Díez-Minguito,
mdiezm@ugr.es

Citation:
Díez-Minguito, M., A. Baquerizo, H. E. de Swart, and M. A. Losada (2014), Structure of the turbidity field in the Guadalquivir estuary: Analysis of observations and a box model approach, *J. Geophys. Res. Oceans*, *119*, 7190–7204, doi:10.1002/2014JC010210.

Received 3 JUN 2014
Accepted 26 SEP 2014
Accepted article online 6 OCT 2014
Published online 27 OCT 2014
Corrected 8 JAN 2015

This article was corrected on 8 JAN 2015. See the end of the full text for details.

Abstract A study is presented on the transport of suspended particulate matter (SPM) in the Guadalquivir estuary during low river flow conditions. Observations show that tidally induced SPM exceeds that associated with catchment-derived inputs. The main mechanisms that contribute to longitudinal transport are identified and quantified by analyzing the tidally averaged and depth-integrated SPM flux decomposition over time and space. The net transport is generally directed upstream, although differences in the direction between spring and neap tides are identified. The transport is largely controlled by the mean advection, the tidal pumping associated with the covariance between SPM concentration and current, and the tidal Stokes transport. The convergence of the transport associated to these mechanisms alone explains the presence of primary and secondary estuarine turbidity maxima. The tidal reflection at the upstream dam appears to play a significant role in their generation, as evidenced by the convergence zones of the M4 and M2 induced tidal pumping transports. The spatial structure of the transport motivates the development of a box model that describes the concentration of SPM and its exchange between different stretches along the estuary at subtidal time scales. The model is fed by the net SPM transport obtained from observations. Analysis of the morphodynamical state of the estuary using the box model indicates that erosion is dominant in the stretches close to the estuary mouth and that this sediment is transported upstream and deposited in the middle part of the estuary. This process is more influential during spring tides than during neap tides.

1. Introduction

Estuaries are transition environments whose waters usually present more turbidity than the adjacent oceanic and continental waters. Turbidity is a measure of the light absorption and scattering in water due to the presence of dissolved organic matter and suspended particulate matter (SPM), typically clay and silt [*Winterwerp and Van Kesteren*, 2004]. The spatiotemporal distribution of turbidity depends on factors like tidal forcing, stratification, and bathymetry, and frequently shows estuarine turbidity maxima (ETM) [e.g., *Talke et al*., 2009b; *Lin and Kuo*, 2001; *Kappenberg and Grabemann*, 2001; *Uncles*, 2002].

The dynamics of the suspended particulate matter is important to the functioning of the estuarine ecosystems and of the adjacent coastal area [*Eisma*, 1993]. High turbidity levels usually have negative consequences on water quality, and thus on economy and society. The lack of light in the water column is a vital limiting factor in the production of biomass [*Cloern*, 1987; *Talke et al*., 2009a]. This is indeed the case of the Guadalquivir estuary, which exhibits high suspended sediment concentrations, and frequently has water quality problems throughout the year. In the last decade, several events of high turbidity during long periods with almost no freshwater discharge from the upstream dam led to hypoxia. There is evidence that the strong light attenuation (caused by the high turbidity) inhibited the phytoplankton growth in the water column [*Navarro et al*., 2012]. This low photosynthetic biomass, which yielded low rates of photoautotrophic oxygen production, together with high rates of oxygen consumption by the large input of organic material into the estuary, resulted in a water column where oxygen consumption dominated over oxygen production [*Ruiz et al*., 2014]. In addition, human activities in the estuary, like fishing, aquaculture, commercial navigation, irrigation returns, and dredging works, influence both the morphological and sedimentological evolution and water quality [see e.g., *Johnston*, 1981; *de Jonge*, 1983; *Hickey et al*., 2010; *Losada and Ruiz*, 2010; *de Jonge et al*., 2014].

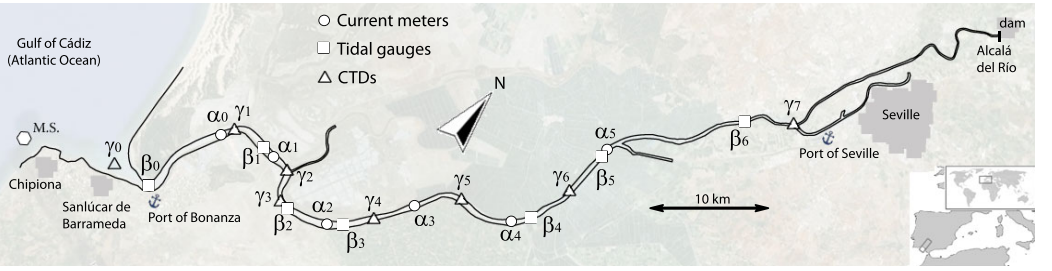

Figure 1. Study area. The map includes the stations of the RTMN analyzed in this work. These are current meter (circles, α_i), tidal gauges (squares, β_i), and water quality probes or CTDs (triangles, γ_i). The origin of the along-channel axis is considered at station γ_0. The RTMN includes a meteorological station (M.S.) off Chipiona.

Regarding this overall context, it is therefore crucial to identify and quantify the mechanisms controlling SPM dynamics. In this sense, the availability of physically inspired models based on observations permits the identification of the principal control mechanisms of the SPM, and to gain insight into the morphological state of the estuarine system. With this general purpose in mind, this work presents a thorough analysis of the observations recorded between 2008 and 2011 by a Real Time Monitoring Network (RTMN) [*Navarro et al*., 2011]. Observed along-channel transport rates are determined during low river flows, and used to force a box model [see e.g., *Hagy and Murrell*, 2007; *Amos and Tee*, 1989; *Officer*, 1980; *Pritchard*, 1969] of a suspended load balance at tidally averaged scales.

The model, applied to six neighboring stretches whose lengths are of the order of the tidal excursion, determines the SPM concentration as the solution of a linear system of equations, which represents the SPM conservation in several interconnected segments of the estuary. The model is used to assess the morphological state of the estuary by estimating how much SPM in each box or segment deviates from its equilibrium value. The joint analysis of the observations and results of the model permits the evaluation of the sediment balance and the structure of the turbidity field. Moreover, it allows for the identification of the control mechanisms in the SPM transport in the low and middle part of the estuary at a tidally averaged scale and under low river flow conditions.

In the following sections, the study area and the instrumentation are described in detail (section 2), along with the decomposition of the advective transport and an outline of the box model (section 3). Section 4 presents the observations and the analyses of the longitudinal transport of SPM and the morphodynamic equilibrium state of the system. Finally, in section 5 the results and their possible implications and limitations are discussed, and in section 6 the most important conclusions of the work are listed.

2. Background

2.1. Study Area

The Guadalquivir estuary (36°43′N– 37°32′N, 5°56′W–6°30′W) is a transition area between the basin of the river of the same name and the Gulf of Cádiz (Figure 1). The estuary comprises the last 110 km of the Guadalquivir river, 85 of which are navigable as far as Seville. The mean depth of the principal channel is approximately 7 m. Cross sections, A, decrease exponentially upstream, i.e., $A=A_0\exp\{-x/\lambda\}$, with $A_0=5839.4\text{m}^2$, a convergence length of $\lambda=60\text{km}$, and x measures the distance to the mouth of the estuary [*Díez-Minguito et al*., 2012].

The bed of the upper reach of the estuary is over 90% composed of fine-grained muds ($D50 \sim 0.003\text{mm}$), while in the rest of the estuary a typical distribution is 80% of sand and 20% of silt and clay ($D50 \sim 0.2\text{mm}$). The concentration of solids in suspension usually varies between 0.5 and $4.5\text{kg}/\text{m}^3$. Values at the near-surface as high as $16\text{kg}/\text{m}^3$, triggered by discharges from the upstream dam, may also be found [*Contreras and Polo*, 2012].

The tide in the Guadalquivir estuary is semidiurnal, as indicated by the relation between the greatest diurnal and semidiurnal amplitudes ($F \approx 0.1$), and the range is mesotidal, below 4 m at the mouth. The wave propagation is dominated by friction in the lower stretches of the estuary, which is the part in which it exhibits more tidal flats, and in the upper part by tidal wave reflection at the Alcalá del Río dam. In the middle part,

Table 1. CTD Locations (γ_i) in Geographical Coordinates and Positions in km With Respect to the Estuary Mouth[a]

Station	γ_0	γ_1	γ_2	γ_3	γ_4	γ_5	γ_6	γ_7
km	0	17.30	23.60	26.20	35.30	47.10	57.60	84.30
lat° N	36.75	36.87	36.91	36.89	36.94	37.03	37.11	37.32
lon° W	6.39	6.34	6.28	6.25	6.19	6.13	6.08	6.00
$\bar{c}_0^{th}$ (kg/m^3)	0.40	0.93	1.18	2.38	2.08	1.46	2.80	2.05

[a]The last row shows the estimated tidally averaged SPM thresholds, $\bar{c}_0^{th}$, between low and high river flow conditions.

the balance between terms related to convergence and friction in the tidal wave propagation equations give rise to a synchronous behavior [*Díez-Minguito et al*., 2012].

Under normal or low river flow conditions, i.e., with freshwater flows below 40m^3/s, this is a tidally energetic estuary, which results in well-mixed conditions, except for a partial stratification in the mouth area. A vertically sheared circulation is observed, but its effects on the salt transport are clearly lesser than the tidal effects [*Díez-Minguito et al*., 2013]. The analysis of the stratification-circulation parameters under normal conditions establishes a Type-2a estuary according to the scheme of *Hansen and Rattray* [1966]. The null point of the tidally averaged saline intrusion is normally around 70 km. Occasionally, it has reached the Port of Seville, but never the Alcalá del Río dam [*Díez-Minguito et al*., 2012]. The estuary is positive under all circumstances; its freshwater inputs being sufficient to compensate for its evaporation losses. With fluvial discharges above 400m^3/s, which occur sporadically, the estuary is considered to be dominated by fluvial dynamics, and it features a discharge plume with a salt-wedge structure at its mouth.

2.2. Measurements

For 3 years (from February 2008 onward), extensive monitoring of its turbidity was carried out in the estuary by the installation by the Institute for Marine Sciences of Andalusia (ICMAN-CSIC) of an extensive remote real-time monitorization network [*Navarro et al*., 2011]. The instruments were moored at places close to the main axis of the navigation channel.

Eight environment quality Conductivity-Temperature-Depth stations (CTD) (denoted by γ in Figure 1) were set up between 0 and 84.30 km (Table 1). The origin of the along-channel axis, x, positive upstream of the estuary, is defined at station γ_0, situated at the estuary mouth. Among other physicochemical variables, the CTDs recorded turbidity, conductivity, and temperature. The sampling period of the CTD probes was 30 min and at some intervals, 1 h. During the first 9 months, the CTDs took samples at four different depths ($z=-1,-2,-3$, and -4m) with respect to the free surface. As from November 2008 onward, for technical reasons, measurements were taken only at $z=-1$m. Suspended matter concentration, c, is calculated in this work in kg/m^3 from turbidity data observed in formazine nefelometric units (fnu). The calibration of the samples established a relation between particulate matter concentration and fnu of $(1.60\pm0.15)\times10^{-3}$ kg/m^3/fnu [*Navarro et al*., 2011], where the error bar represents the 95% confidence interval. Accuracy of concentration values is thus of order $100(1.60-0.15)/1.60 \approx 90\%$.

Besides turbidity measurements, sea level and current profile data were also collected (Figure 1). The current meters recorded velocity profiles every 15 min from $z=-1$m down to $z=-7$m, with cells of 1 m. According to the current-rose diagrams, the along-channel current is considered to be accurate to within 10%. Error propagation from uncertainty in the concentration and current measurements is calculated according to standard variance formula. Daily data of discharges from the Alcalá del Río dam were provided by the Agencia Andaluza del Agua (Junta de Andalucía).

3. Formulation and Methodology

3.1. Longitudinal Advective Transport

With the aim of identifying and quantifying the different mechanisms contributing to the transport of SPM under low river flows, the tidally averaged flux, is determined at several specific points of the navigation channel at five different depths. Assuming that for a generic variable ξ, $\bar{\xi}$ represents the average of a

semidiurnal cycle M2, ξ can be decomposed as $\xi=\bar{\xi}+\tilde{\xi}$, $\tilde{\xi}$ being the deviations with respect to the tidally averaged value. The tidally averaged advective flux, $\overline{f_c}$, is thus determined as

$$\overline{f_c} = \overline{uc} = \bar{u}\bar{c} + \overline{\tilde{u}\tilde{c}}, \tag{1}$$

where u is the along-channel velocity, and c is the SPM concentration [*Becker et al*., 2009; *Dyer*, 1997]. The first term on the right-hand side of equation (1) represents the mean or residual advective flux, whereas the second one is associated with processes dependent in time [*Scully and Friedrichs*, 2007; *Jay and Smith*, 1990].

Various authors used the tidally averaged and depth-integrated flux to obtain additional information on the mechanisms controlling solute transport in the whole water column [*Uncles et al*., 1985; *Jilan and Kangshan*, 1986; *Dyer*, 1997; *Wai et al*., 2004; *Li et al*., 2014]. The transport rate of c through a cross section of unit width (f_c vertically integrated) is

$$T_c = \int_{-h_0}^{\eta} f_c\, dz = \int_{-h_0}^{\eta} uc\, dz, \tag{2}$$

where the height of the water column is $h=h_0+\eta$, h_0 is the reference depth, and η is the elevation of the free surface. The tidally averaged transport rate is

$$T \equiv \overline{T_c} = \underbrace{\bar{h}\bar{u}\bar{c}}_{\tau 1} + \underbrace{\bar{c}\overline{\tilde{\eta}\tilde{u}}}_{\tau 2} + \underbrace{\bar{u}\overline{\tilde{\eta}\tilde{c}}}_{\tau 3} + \underbrace{\bar{h}\overline{\tilde{u}\tilde{c}}}_{\tau 4} + \underbrace{\overline{\tilde{\eta}\tilde{u}}\,\overline{\tilde{c}}}_{\tau 5} + \underbrace{\bar{h}\overline{\tilde{u}_v\tilde{c}_v}}_{\tau 6} + \underbrace{\bar{h}\bar{u}_v\bar{c}_v}_{\tau 7} + \underbrace{\overline{\tilde{\eta}u_vc_v}}_{\tau 8}. \tag{3}$$

Here $\underline{\xi}$ represents the depth-averaged value of ξ performed over the local mean depth and ξ_v the deviation at each depth with respect to that value, i.e., $\xi=\underline{\xi}+\xi_v$. The term $\tau 1$ in equation (3) represents the nontidal transport induced by the depth-mean net current. The term $\tau 2$ is associated with the tidal Stokes transport, while $\tau 3$–$\tau 6$ are tidal pumping terms generated by positive or negative correlations between the tidal oscillations of $\underline{c}$, $\underline{u}$, and η. The term $\tau 7$ accounts for vertically sheared mean flow, and term $\tau 8$ is associated with the triple correlation between η and the intratidal deviations with respect to the depth-averaged values of u and c. The interval analyzed is limited by the availability of simultaneous data of elevations, turbidity, and currents, at all depths and stations, and comprises two neap tides and two spring tides (from 22 July 2008 to 16 August 2008).

3.2. Box Model: SPM Balance in a Control Volume

The morphodynamic state of the estuary is analyzed with a semianalytical model for longitudinal transport which, by means of the mass conservation equation, established a net balance of SPM per stretch at a subtidal scale. The relative difference between the suspended masses observed and those obtained with this model under balance conditions is a simple measurement of how each stretch of the estuary deviates from the equilibrium conditions and it permits a discussion on the general morphodynamic trend of the system.

The mass balance equation for the suspended matter is expressed as

$$\frac{\partial c}{\partial t} + \frac{\partial F_k}{\partial x_k} = 0. \tag{4}$$

Here Einstein's summation convention is adopted. The fluxes, which comprise advective and diffusive contributions, are

$$\begin{aligned} F_x &= uc - K_h \frac{\partial c}{\partial x}, \\ F_y &= vc - K_h \frac{\partial c}{\partial y}, \\ F_z &= (w - w_s)c - K_v \frac{\partial c}{\partial z}, \end{aligned} \tag{5}$$

with $\{x, y, z\}$ the three Cartesian directions, and (u, v, w) the components of the three tridimensional current vector. Furthermore, K_h and K_v are, respectively, the horizontal and vertical turbulent diffusion coefficients, and w_s the sediment fall velocity.

The volume integral of equation (4) over stretch i, according to Gauss theorem and the Leibniz rule, yields

$$\frac{\partial}{\partial t}\iiint_{V_i} c dV + \iint_{S_i} \Phi_k n_k dS = 0, \tag{6}$$

in which V_i is the volume and S_i its surface. In this equation, $\Phi_k = F_k - cw\delta_{k,3}$ are the fluxes in the three Cartesian directions $\{x, y, z\}$ and $\delta_{\mu,\nu}$ is the Kroneker delta.

Equation (6) is applied to the Guadalquivir estuary, segmented in $N = 6$ stretches, defined by intervals $(x_i, x_{i+1}), i = 1, 2, \ldots, N$, where x_i are the locations of the γ_i, i.e., $x_1 = 0\text{km}, x_2 = 17.3\text{km}, x_3 = 23.6\text{km}, x_4 = 26.2\text{km}, x_5 = 35.3\text{km}, x_6 = 47.1\text{km}$, and $x_7 = 57.6\text{km}$. Taking into account that the boundary conditions that express that fluxes must vanish on the margins and at the surface, equation (6) can be expressed as

$$\frac{\partial m_i}{\partial t} + \iint_{A_{i+1}} F_x dA - \iint_{A_i} F_x dA - \iint_{\mathfrak{A}_i} (E - D) dA = 0, \quad i = 1, 2, \ldots, N, \tag{7}$$

where m_i is the mass in suspension in each stretch, A_i the cross-sectional area in x_i, $\mathfrak{A}_i$ is the bed area of the box V_i, and the last term represents the balance between erosion, E, and deposition, D.

3.3. Suspended Mass Under Stationary Conditions

Assuming that the system is stationary [*Friedrichs et al.*, 1998], equation (7) is reduced to

$$\iint_{A_{i+1}} \widehat{F}_x dA = \iint_{A_i} \widehat{F}_x dA \quad \text{for } i = 1, \ldots, N, \tag{8}$$

in which the symbol $\widehat{\cdot}$ above the variables denotes their values under stationary conditions. More details on the calculation are given in Appendix A. The fluxes of SPM at the boundaries between the different boxes can be decomposed in advective and diffusive contributions ($\widehat{F}_x = \widehat{F}_x^{(adv)} + \widehat{F}_x^{(dif)}$). The advective term is estimated according to

$$\iint_{A_i} \widehat{F}_x^{(adv)} dA = \left(\widehat{bT}\right)_i, \tag{9}$$

where b is the width and T is the SPM transport per unit width, both evaluated at stretch i. Numerically, the diffusion term is estimated using first-order finite differences, that is

$$\iint_{A_i} \widehat{F}_x^{(dif)} dA \approx -\frac{2K_{h,i}}{\Delta_{i-1}^{i+1}} \left(\frac{\widehat{m}_i}{\Delta_i^{i+1}} - \frac{\widehat{m}_{i-1}}{\Delta_{i-1}^{i}} \right), \tag{10}$$

with $K_{h,i}$ an effective longitudinal dispersion coefficient, $\Delta_\nu^\mu \equiv x_\mu - x_\nu$, and no summation convention is used here. The result is a diffusive transport which depends on the suspended sediment masses under stationary conditions, $\widehat{m}_i$. The values $K_{h,i}$ employed are $K_{h,i} = 1754\,\text{m}^2/\text{s}$ for $i = 5, 6$ and $K_{h,i} = 963\,\text{m}^2/\text{s}$ for the rest of the boxes, similarly to those obtained for salinity in *Díez-Minguito et al.* [2013]. A sensitivity analysis is performed on these parameters. At the upstream boundary, station x_7, a vanishing diffusive flux is imposed.

3.4. Closing Conditions

For given values of b_i and $\widehat{T}_i$ at γ_i, the application of equation (8) for each box results in a system of N linear equations whose unknowns are the suspended sediment masses in equilibrium $\{\widehat{m}_i\}_{i=1}^N$. However, under low river flow conditions, the sediment supplied by the freshwater discharge is small compared to the amount of SPM observed inside the estuary. This suggests the following constraint for the masses at equilibrium: $\sum_{i=1}^{N} \widehat{m}_i = M$, where M is the total suspended sediment mass estimated from the turbidity measured at the different stations. This relationship reduces the problem to solving the set of equations (8) for $i = 2, \ldots, N$ and, consequently, it avoids the specification of the transport at the estuary mouth.

4. Results and Analysis

Figure 2 (inset) shows a typical temporal series of near-surface turbidity at a midestuary point. The variability of the signal permits the identification of several harmonic components, which result from different

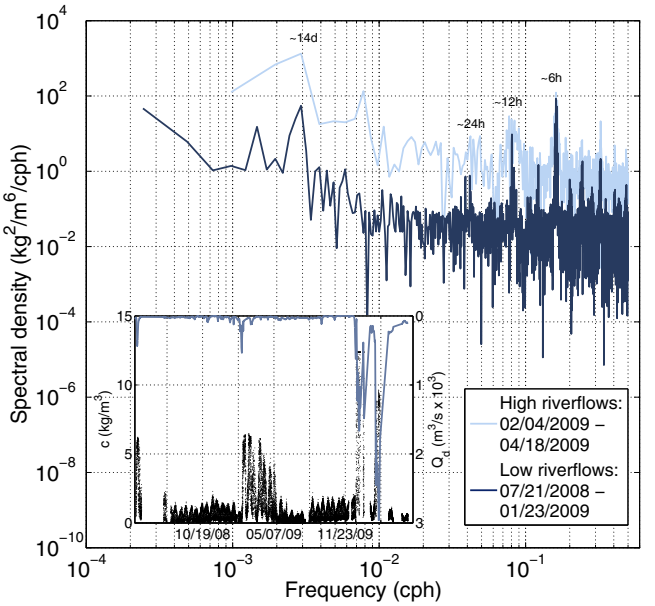

Figure 2. Spectral content of near-surface turbidity series during low river flows (dark blue curve) and after high freshwater discharges (light blue curve) at station γ_5 on the dates shown. Several frequency peaks are labeled. Inset: Time series of surface turbidity at γ_5 (dots, left-hand vertical axis) and discharges from the Alcalá del Rio dam (right-hand inverted vertical axis, solid line) during the same period.

forcings, among them, the intratidal variations and the spring-neap tide cycles (e.g., around 19 October 2008). The peaks in the spectrum at near fortnightly, semidiurnal, and diurnal scales point to a mainly tidally driven turbidity. The presence of highly energetic overtides (∼6h and shorter periods) visible in Figure 2 shows the marked nonlinear character of the generating mechanisms, especially the frictional ones. The ratios between the spectral densities at quarter-diurnal and semidiurnal frequencies for different locations are shown in Table 2. The spectral density associated with the quarter-diurnal components exceeds that associated with the semidiurnal constituent at γ_4, γ_5, and, especially, at γ_6. The latter location coincides with the presence of a node in the M4, attributed by *Díez-Minguito et al*. [2012] to tidal reflection at the Alcalá del Río dam.

The structure of the intratidal turbidity and current fields shown in Figure 3 supports the view of a system in which turbidity is mainly generated by tidal erosive fluxes. The amount of sediment suspended in the water column (first plot) is larger after the occurrence of the maximum flood (second plot), which exhibits a negative lag with respect to high water due to the effect of friction. The resuspension capacity of the bed material by turbulence generation is less during ebb conditions, which is consistent with a flood-dominated estuary [*Díez-Minguito et al*., 2012].

4.1. Time Series: SPM Regimes

The analysis of the data shown above reveals two regimes for the turbidity in the estuary. One *Normal* during low river flow conditions, with turbidity values ranging in accordance with the ebb-flood and spring-neap tide cycles. The characteristics of these patterns do not change between different spring-neap cycles. The results and analysis of this work correspond to this regime. The other regime, called *Extreme*, which is typically triggered by discharge events from the upstream dam (see inset Figure 2), is transitional and is characterized by turbidity values that are one to several orders of magnitude higher than the former in practically the entire estuary. The data collected by the RTMN suggest the threshold values for the near-surface tidally averaged concentrations, $\bar{c}_0^{th}$, shown in Table 1. These thresholds, which vary spatially depending on the cross section in the estuary, allow for distinguishing and studying separately the two turbidity regimes (*Normal* and *Extreme*). This is convenient since the control mechanisms, origin, and distribution of the sediment can be different. The threshold values are estimated as 20% larger than the maximum value observed during Normal, low river flow conditions. Values at $z=-4$m are approximately a factor two larger.

Table 2. Spectral Density Ratio Between M4 and M2 Components of the Turbidity During 21 July 2008 to 23 January 2009

Station	γ_0	γ_1	γ_2	γ_3	γ_4	γ_5	γ_6	γ_7
E_{M4}/E_{M2}	0.068	0.29	0.17	0.11	1.22	8.83	29.23	0.10

4.2. Spatiotemporal Distribution of the Subtidal Turbidity Field

Figure 4 shows typical tidally averaged turbidity and salinity profiles at spring and neap tides. The spatial patterns indicate that turbidity tends to increase

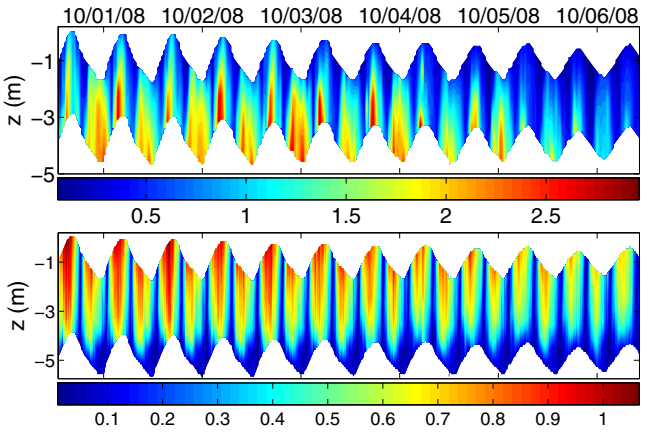

Figure 3. (top) Turbidity $c(z, t)$ in kg/m^3 recorded at station γ_4, and (bottom) magnitude of the longitudinal current $|u(z, t)|$ in m/s in α_3 in a complete cycle of spring-neap tides during low river flows. The elevation (m) is that observed at the point β_3.

upstream of the estuary. During neap tides (27 August 2008, plots a1 and a2), the tidal currents resuspend less sediment than in spring tides and the largest (primary) ETM is observed around 80 km ($\approx 1\,\mathrm{kg/m^3}$ at $z=-4$ m), which is the location up to which measurements are available. This maximum may well correspond to the classic turbidity optimum due to the salt intrusion null-point (second plot) [*Postma*, 1967]. The fact that the primary ETM appears around the null point during neap tides could be due to the relative decrease in the vertical turbulent mixing. At 35 km ($\approx 0.86\pm0.08\,\mathrm{kg/m^3}$ at $z=-4$ m) and around 58 km ($\approx 0.99\pm0.09\,\mathrm{kg/m^3}$ at $z=-4$ m) secondary turbidity maxima appear, which may be generated by the tidal reflection in the upstream dam. The ETM at 35 km has been also detected using the DEIMOS-1 satellite imagery [*Caballero et al.*, 2014].

The concentrations during spring tides (3 September 2008, plots b1 and b2 in Figure 4) are a factor two or three larger than those observed in neap tides. Specially notable is the increase in the maxima found at 58 km ($c(x=58\,\mathrm{km}, z=-4\,\mathrm{m}) \approx 3.0\pm0.3\,\mathrm{kg/m^3}$) and 35 km ($c(x=35\,\mathrm{km}, z=-4\,\mathrm{m}) \approx 2.26\pm0.21\,\mathrm{kg/m^3}$), whose turbidity exceeded that generated near the saline intrusion point ($c(x=80\,\mathrm{km}, z=-4\,\mathrm{m}) \approx 1.61\pm0.15\,\mathrm{kg/m^3}$). The primary-secondary character of the ETMs thus changes from neap to spring tides. The locations of these two ETM, at 58 km and at 35 km, persist during other tidal cycles, although their magnitudes varied with the tidal range and the fluvial discharge.

4.3. Along-Channel SPM Transport

A more quantitative characterization of the mechanisms generating the turbidity maxima is made by using equation (3). The top plot of Figure 5 shows the along-channel SPM transport in each spring and neap tide cycle. The bottom plot of the same figure shows the transport, net and decomposed into its eight terms, during the analyzed time period (22 July 2008 to 16 August 2008).

During spring tides (Spring 1 and Spring 2 periods, top plot), the magnitude of the transport is, in most of the stations and within the margin of the error bars, larger than that found during neap tides (Neap 1 and Neap 2 periods). This is a consequence of the larger advection capacity of the tidal flow and of the larger amount of SPM available, as a result of the higher bed shear stress at the bottom. This causes the structure of the along-channel net transport during the analysis period (bottom plot, squares, black line) to be similar to that observed during spring tides. The largest transport convergence zone is found between 25 and 35 km, where the transport changes its sign.

During neap tides (Neap 1 and Neap 2 periods, top plot) the convergence of transports weakens significantly and the downward zero-crossing of the transport shifts upstream. It might even disappear, according to the uncertainty in the results. This behavior is consistent with the significant reduction in the turbidity observed in the first local maximum during the neap tides in relation to other positions (Figure 4, bottom). The transport observed both during the spring and during the neap tides at γ_5, 47 km, (γ_6, 57.6 km) remains negative (positive). However, at γ_4 (35.30 km), the transport changes its sign from spring to neap. The differences in the direction of the transport between spring and neap tides were already observed in other estuaries [*Blanton et al.*, 2003; *Becker et al.*, 2009]. The predominantly positive sign of the transport near the estuary mouth favors the trapping of fine sediments inside the estuary.

Figure 5 (bottom) shows the different terms that constitute the total mean transport, as described by equation (3). The terms $\tau1, \tau4$, and $\tau2$, ordered by their relative importance, explain 98% of the suspended matter transport in the Guadalquivir estuary. Within the error bars, their modal net values range

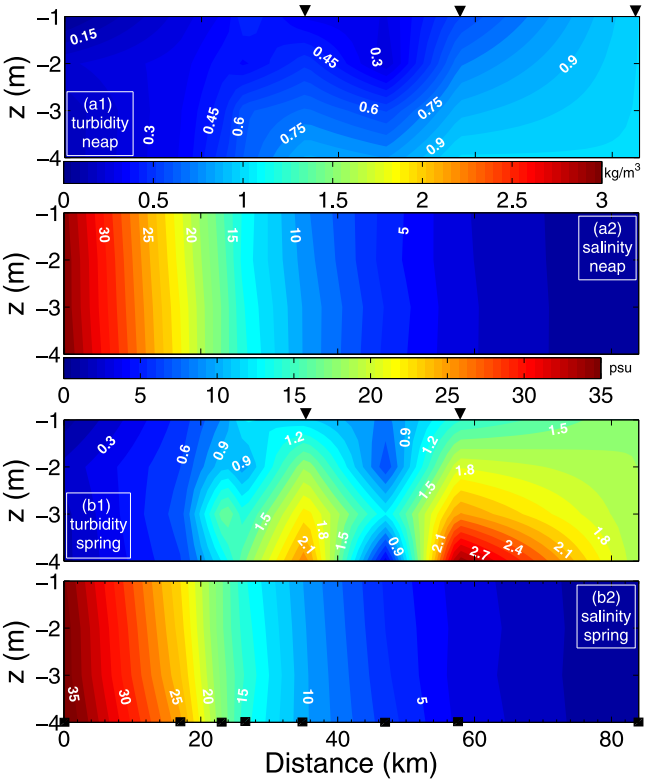

Figure 4. Turbidity field $c(x, z)$ (in kg/m^3) and salinity $s(x, z)$ (in psu) averaged 48 h during neap tides (from top to bottom: first and second plots, respectively) and during spring tides (third and fourth plots, respectively) interpolated taking the data available on the dates indicated. The color scale is the same for spring and neap tides. The arrow tips in the top of the plots show the positions of the primary and secondary ETM. The black squares in the bottom of the last plot indicate the CTD locations.

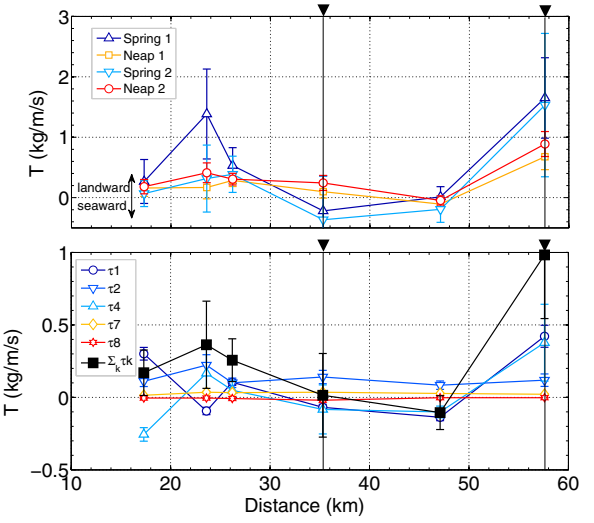

Figure 5. (top) Net transport during the periods of time 22 July 2008 (Spring 1), 26 July 2008 to 28 July 2008 (Neap 1), 01 August 2008 to 03 August 2008 (Spring 2), and 07 August 2008 to 09 August 2008 (Neap 2). (bottom) Net transport (squares, black line) during the whole analyzed time period (22 July 2008 to 16 August 2008) and its terms. Only the five largest terms are shown ($\tau 3$, $\tau 5$, and $\tau 6$ are omitted here for clarity). The arrows indicate the direction of the net transport. In both plots, positive (negative) values denote estuary transport upstream (below). The vertical lines and the arrow tips in the top of the plots indicate the locations of the ETM observed.

throughout the entire estuary, respectively, between -0.13 kg/m/s (attained at station γ_5) and 0.42kg/m/s (at γ_6), between -0.25kg/m/s (at γ_1) and 0.37kg/m/s (at γ_6), and between 0.08kg/m/s(at γ_5) and 0.22kg/m/s (at γ_2). The term $\tau 1$, associated with the nontidal transport, accounts for 45% of the total transport. The term $\tau 4$ represents 37% of the total transport and exhibits a longitudinal variation which resembles that of the net transport. The term $\tau 4$ stands for the transport induced by the phase lag between the current and the sediment concentration due to the asymmetry in erosion during the tidal cycle, the asymmetry in mixing, and the spatial and temporal settling lag [*Wai et al.*, 2004; *Dyer*, 1995; *Jay and Musiak*, 1994; *Uncles et al.*, 1985]. The term $\tau 4$ changes its sign 3 times along the estuary, which is caused by changes in the relative phases of u and c. The other tidal pumping terms ($\tau 3$, $\tau 5$, and $\tau 6$) are of a lower order of magnitude than $\tau 4$. The third is the term $\tau 2$, associated with Stokes transport, which favors upstream sediment transport.

These three mechanisms are the same as those which generate most of the salt transport in this estuary [*Díez-Minguito et al.*, 2013]. However, regarding sediment transport, the term $\tau 4$ is almost as important as $\tau 1$, being over $\tau 2$. This is a result of the lags in the response of the sediment to the flow. In view of the magnitude of each term $\tau 1, \ldots, \tau 8$, it can be concluded that the vertically sheared mean flows represent a lesser contribution to the generation of turbidity maxima.

Finally, and in relation to the net SPM transport during the analysis period (Figure 5, bottom), the convergence of the transport explains the presence of the ETM located at 35 km (more clearly during spring tides). This secondary maximum is close to where the net transport vanished and the convergence of transport is large. Identical behavior occurred near the primary ETM found around 58 km. In fact, a net landward transport downstream of the maximum is observed. However, the lack of any current meters upstream from this position does not permit the identification of any possible seaward transport upstream from the ETM. Around 50 km, the net sediment transport again vanished, but the transport is divergent. In this zone a turbidity minimum, flanked by relative maxima at 35 and 58 km (see Figure 4), is observed.

4.4. Deviation From Morphodynamic Equilibrium

The structure of the transport shown in the previous section leads to an integrated formulation in which the sediment is transported by advection and dispersion between the different stretches of the estuary. From the transport given by equation (3) in each tidal cycle the system of linear equations (see section 3.2) is solved obtaining the distribution of masses in each stretch for equilibrium conditions, $\{\widehat{m}_i\}_{i=1}^{N}$. Error estimates for the equilibrium masses are thus derived from the uncertainty in the transport.

The temporal variability of the relative difference between the masses observed (m_i) and those obtained with the model in each estuary stretch under stationary conditions ($\widehat{m}_i$), i.e., $(\widehat{m}_i - m_i)/m_i$, is a simple way to quantify to what extent each stretch deviates from equilibrium conditions. The (normalized) tidally averaged masses observed (Figure 6, middle) are estimated by using the measurements of the SPM concentration, c_i, averaging it in the water column and in each tidal cycle, and assuming boxes with a rectangular prismatic geometry, i.e., $m_i = c_i V_i$.

Generally, there is a nonvanishing relative difference between the masses observed and those obtained with the equilibrium model (Figure 6, bottom). Apparently, the general distribution is that the relative difference decreased upstream, going from positive values in the lower stretches to negative in the upper stretches. Positive values (stretches $\gamma_0 - \gamma_1$ and $\gamma_1 - \gamma_2$) mean that, during the time analyzed, the masses observed are lower than those in equilibrium, indicating that part of the sediment deposited should go back to the water column in order to return the system to a balanced situation. The negative values exhibited by the stretches from $\gamma_2 - \gamma_3$ to $\gamma_5 - \gamma_6$ during almost the whole analysis interval, reveal the existence of an excess of suspended sediment. So in order to return to the equilibrium, the system favors deposition in those stretches.

Temporal variability is observed in the curves in Figure 6. This is associated with the diurnal inequality and fortnightly cycles (spring-neap) inherited from the variability observed in masses and transport. During the spring tide after 31 July 2008 the differences observed are larger than those in the rest of the record. The relative difference in masses in the first stretch almost reaches a factor 2, while already in the second stretch it is below 1. In the rest of the stretches upstream, the differences (<0) vary from -0.1 in the third stretch to nearly -1 in $\gamma_5 - \gamma_6$. During neap tides (around 26 July 2008 and 10 August 2008), the magnitude of the relative differences in all the segments of the estuary decreases between 65% and 35%. During some specific tidal cycles the estuary seemed to be closer to morphological equilibrium. A change of sign in $(\widehat{m}_i - m_i)/m_i$ in some stretches is even observed (see e.g., deviations in stretches 1 and 6 on 26 July 2008) due to variations in the nontidal transport.

Taking the deviations $\widehat{m}_i - m_i$ in each stretch $i = 1, \ldots, 6$, an estimate can be made of the equivalent eroded/deposited bed height, which is a more intuitive quantity. The sediment density is $\rho_s = 2650 \mathrm{kg/m^3}$ and a volume fraction of sediment $\phi_s = 0.15$ is assumed [*Sanford and Maa*, 2001]. Additionally, it is assumed that the erosion/deposition in the stretch is uniform in the whole bed. Taking into account these simplifications, the variation in the position of the bed Δz_i for the first (erosive) and last (depositional) stretches at the tidal cycle around 31 July 2008, for example, is $\Delta z_1 = +(3.2 \pm 1.7)\mathrm{cm}$ and, $\Delta z_6 = -(1.8 \pm 1.5)\mathrm{cm}$, respectively. Similar values were observed in the Hudson river [*Traykovski et al.*, 2004]. Bed height variations during neap tidal cycles are much lower.

In order to test how sensitive are the results to the dispersion coefficients, a sensitivity analysis is performed. The box model is run for a set of values within the intervals $K_{h,i} = (963 \pm 500)\mathrm{m^2/s}$ for $i = 1-4$, and $K_{h,i} = (1754 \pm 250)\mathrm{m^2/s}$ for $i = 5, 6$ [*Díez-Minguito et al.*, 2013]. The analysis indicates that the general trend is maintained: the relative difference between the masses observed and those obtained with the box model

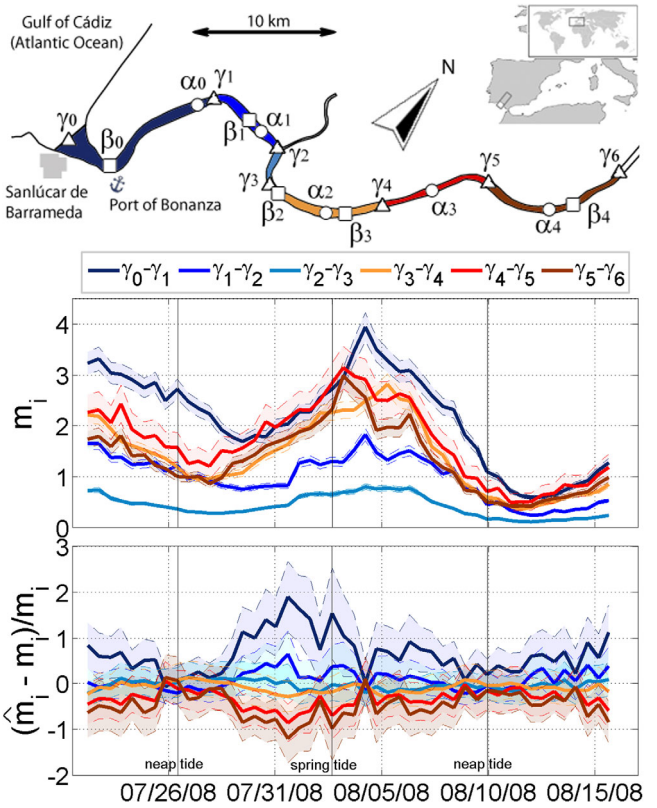

Figure 6. (top) Study area with shaded, colored stretches for reference. (middle) Tidally averaged observed mass m_i in each stretch i. Masses are nondimensionalized by $M_{ref}=10^8$ kg. (bottom) Relative difference between observed mass m_i and equilibrium mass from the model $\hat{m}_i$. Error bars in middle and bottom plots are depicted as shaded areas.

decreases upstream, going from positive values in the outermost stretches to negative in the innermost stretches. The magnitude, however, may change. During spring tides the differences are more evident. If the lower endpoints of each interval are employed, the magnitude of the relative difference almost doubles. The model is less sensitive to an increase in $K_{h,i}$ (reduction of 10% in magnitude for the upper endpoints). Nevertheless, the deviation of the results with regards to those using the midpoints (see Figure 6) is of the same order of magnitude than the errors due to the uncertainty in current and concentrations. There is considerable overlap of the error bars from uncertainty estimation for the different tested cases.

Despite not having any reliable data at the bed-water interface, the model is tested with the differences between the erosion and sedimentation rates estimated by a boundary-layer model for cohesive sediments [*Winterwerp and Van Kesteren*, 2004]. The erosion/deposition formulation of *Son and Hsu* [2011] and *Sanford and Halka* [1993] is adopted here. The erodibility of the bed can be expressed (in m/s) as

$$E=\max\{\beta_e(\tau_b/\tau_c-1),0\}, \tag{11}$$

where $\tau_b=\rho C_D u_{100}^2$ is the bottom shear stress, $C_D=2.5\times10^{-3}$ [*Díez-Minguito et al.*, 2012] is the drag coefficient, u_{100} is the velocity at 1 m above the bed estimated with the current meter data, and $\tau_c(t)=\alpha_1(m-\alpha_2)^{\alpha_3}$ is the critical shear stress (in Pa), which includes the bed consolidation effects [*Sanford and Maa*, 2001]. Here the total suspended mass per unit area observed in each stretch is m and α_1, α_2, α_3, and β_e are empirical parameters. Standard values for these parameters available in the literature are taken, viz., those estimated by *Son and Hsu* [2011]. These are $\alpha_1=0.45\text{kg}^{1-\alpha_3}/\text{s}^2/\text{m}^{1-2\alpha_3}$, $\alpha_2=0.05\text{kg/m}^2$, $\alpha_3=1$, and $\beta_e=3\times10^{-5}$m/s. The sedimentation rate, D, expressed in m/s, is determined as

$$D=\frac{w_d c}{\rho_s \phi_s}\max\{1-\tau_b/\tau_d,0\}, \tag{12}$$

where the deposition velocity for silts is $w_d=2.2$ mm/s, the critical shear for sedimentation τ_d is estimated as a 10% of the critical shear stress for erosion and c is the concentration at the bottom. Maintaining this parameterization in all the stretches, the results indicate the same behavior: the erosion rate is higher in stretches 1 and 2, while the deposition rate exceeds the erodibility of the bed in the rest of the stretches.

5. Discussion

The results and analyses presented here give clues on several issues related to the dynamics of suspended sediment in the Guadalquivir estuary, which are useful from the point of view of managing the environment and which are potentially applicable to other estuaries.

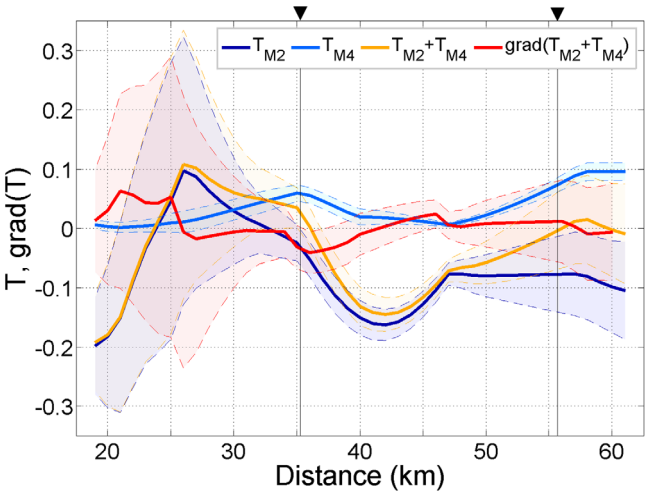

Figure 7. Dark (light) blue curve depicts the transport in kg/m/s associated to the M2 (M4) current-concentration interaction. The orange line shows the net transport $T_{M2}+T_{M4}$, and the red curve shows its spatial derivative in $kg/m^2/s\times10^{-3}$. The vertical lines and the arrow tips in the top indicate the locations of the ETM. Error bars (shaded areas) include here the 95% confidence interval in amplitudes and phases derived from the harmonic analysis of concentrations and currents.

The low river flow regime indicates that most of the observed sediment has as origin the inner estuary and is kept in suspension by bed shear stresses. In fact, comparing the turbidity upstream and downstream of the dam, the latter is a factor 2 larger than the former [*Contreras and Polo*, 2012]. Thus, the amount of sediment discharged from upstream is substantially smaller than that generated locally downstream.

With regard to the distribution of sediment along the estuary, the observations indicate the presence of a primary ETM at 58 km and a secondary ETM at 35 km. Because the estuary is well-mixed under low river flows, these locations cannot be attributed to changes in the vertical structure of the salinity. The persistence of the location of the maxima under different tidal conditions and flows throughout the 3 years of the study also seems to discard a sporadic generation (e.g., due to the effluence of water from adjacent cropping areas), although the topographic influence in its generation cannot be discarded.

The role of the tidal reflection of the M4 constituent in setting the ETMs in the Ems estuary was discussed by *Chernetsky et al*. [2010] and also appears to be important in the Guadalquivir. The harmonic analysis of the horizontal tide identifies that near 58 km there is a maximum for the amplitude of the overtide M4. The velocity trivially vanishes at the foot of the dam. Regarding the vertical tide, the amplitudes of M4 decrease near 58 km (quasi-node), and then increase to reach their absolute maximum at the dam (antinode) [*Díez-Minguito et al*., 2012]. The relationship between elevations and currents for the M4 is typical of a quasi-standing behavior with a node where the primary ETM is observed. With a view to substantiate the role of the tidal reflection on the ETM generation, a harmonic analysis is applied to the depth-averaged turbidity and current time series [*Pawlowicz et al*., 2002]. Amplitudes and phases of the M2 and M4 constituents are obtained and used to compute the transport due to the M4 current-concentration interaction, $T_{M4}=\bar{h}\overline{\underline{u}_{M4}\underline{c}_{M4}}$, and, similarly, the transport due to the M2 constituent alone, $T_{M2}=\bar{h}\overline{\underline{u}_{M2}\underline{c}_{M2}}$ [*Chernetsky et al*., 2010]. The results are shown in Figure 7. The transport due to the M2 (dark blue curve) is negative, except between 24 and 33 km. The M4 transport (light blue curve) tends to move the sediment upstream in all stretches. Its magnitude is larger than the magnitude of the T_{M2} in vicinity of the ETMs. This produces a convergence of transports and thus sediment at the ETMs. This convergence is identifiable by a negative and large longitudinal gradient of the net transport $T_{M2}+T_{M4}$ (red curve). The ETMs also coincide approximately with the downward zero-crossings of the net transport. The tidal reflection thus influences the pattern observed in the distribution of SPM (and other solutes).

The picture of an estuary composed of different segments, each with its own morphodynamic characteristics and exchanging sediment, is the basis of the box model presented here. By quantifying the deviation with respect to the equilibrium state, provided by the model, it is demonstrated that, in general, sediment from the two stretches nearest to the mouth is transferred upstream. In the low stretches, erosion dominates over sedimentation, while in the middle third of the estuary the sedimentation is dominant. The transition between the erosive stretches and those dominated by sedimentation apparently takes place in the third stretch, defined between sections γ_2 and γ_3, where the deviations (although negative on average) are close to zero. It is precisely in this stretch, in which the bends have lowest curvature radius, where the highest longitudinal salinity gradient is observed. This area approximately coincides with the transition between

a diffusive behavior for the tidal wave (in stretches 1 and 2) and with another in which channel convergence and friction compensate each other, i.e., in stretches 3–6 [*Díez-Minguito et al*., 2012]. The box model results are qualitatively consistent with the historical data provided by the Port Authority of Seville between 1964 and 1998, which indicate that the annual volumes of dredged material were larger in the middle and upper stretches [see *Díez-Minguito et al*., 2012].

The limitations presented by the model are, on one hand, the usual ones when adopting a simplified box model representing an idealized section of the estuary [*Officer*, 1980]. The model results are representative of the momentum-conveying part and not of the intertidal areas. Actually, the transport terms feeding the model are determined from the equipment installed in the central section of the navigation channel. On the other hand, morphodynamic equilibrium is assumed, hence no time derivatives are maintained in the model. The unsteadiness of the system is considered in this work by estimating deviations of observed sediment concentrations from their equilibrium values. Nevertheless, in spite of the simplifications, this approach provides valuable information about the short-to-middle term morphodynamic trend of the estuary.

Finally, regarding the vertical structure of the observed fluxes, $\overline{f_c}$, it is predominantly unidirectional, although a slight baroclinic behavior is detected near the mouth. The total seaward (landward) flux evaluated using equation (1) at $z=-1$m ($z=-4$ m) at γ_1 attains a value of $-0.054\mathrm{kg/m^2/s}$ ($+0.075\ \mathrm{kg/m^2/s}$) during the analysis interval 22 July 2008 to 16 August 2008. Conversely, at station (e.g.,) γ_6, the SPM flux is vertically uniform, at least in the upper 5 m of the water column. It is precisely at γ_6 where the largest (smallest) fluxes of SPM (salt) in magnitude are observed, namely, $+0.13\ \mathrm{kg/m^2/s}$ (0.26 psu m/s) at $z=-3$ m.

6. Conclusions

In this work an analysis of the concentrations, fluxes, and transports of suspended sediments during low river flows in a weakly stratified estuary, that of the river Guadalquivir, was presented.

Data observed between 2008 and 2011 show that the estuary displayed moderate-to-high concentrations of SPM during normal conditions. The observed tidally averaged values are smaller than $2.8\ \mathrm{kg/m^3}$ ($4\ \mathrm{kg/m^3}$) at $z=-1$ m ($z=-4$ m), although intratidal concentrations may exceed 4 $\mathrm{kg/m^3}$ ($10\ \mathrm{kg/m^3}$) during spring tide floods.

The correlations between currents and turbidity observed indicate that most of the observed SPM does not originate from the basin but is resuspended by the tidal shear stresses acting at the bed. The observations reveal a complex spatiotemporal structure in the SPM field with the presence of turbidity maxima. During neap tides, the primary ETM is found near the null point (80 km). Secondary maxima are identified at 35 and 58 km. During spring tides, the latter two maxima significantly increase their trapping capacity exceeding that generated near the salinity intrusion point. The primary-secondary character of the ETMs thus changes from neap to spring tides.

The presence of a quasi-node of the M4 vertical tide located at 58 km suggests that tidal reflection in the Alcalá del Río dam is important in setting the ETMs. This is confirmed by the convergence of transport due to the M4 and M2 current-concentration interaction at the ETMs. These locations also coincide approximately with the downward zero-crossings of the net transport.

The net transport rates observed provide additional information on transport mechanisms. The locations of convergence in the longitudinal net transport of SPM correspond well to the ETMs. In particular, transport is predominantly directed up-estuary. Differences in the direction of the transport between spring and neap tides are also observed. The nontidal advection, the tidal pumping associated with the phase lag between the SPM concentration and current, and the Stokes transport, in that order, explain 98% of the total tidally averaged transport. Unlike what is observed with salinity [*Díez-Minguito et al*., 2013], the second mechanism is almost as important as the first mechanism because of the greater lags in the response of the sediment to the flow. The net flow involving vertical shear represents a lesser contribution to SPM transport.

The net transport determined from observations in different estuary stretches and in each tidal cycle serves as input to the box model presented here for SPM. The model, which links dynamically the different stretches (constituting 2/3 of the total length of the estuary), permits an analysis on the morphodynamic state of the estuary under low river flow conditions. The relative difference between the observed SPM masses and those obtained with the box model in each stretch, under stationary conditions, is taken as a simple measure of

how each stretch deviated from the equilibrium conditions. This allows for a first evaluation of the possible consequences of the transport on the morphodynamic balance of the system. The general picture is that in the reaches closest to the mouth, erosion dominated over sedimentation, which predominated upstream.

Appendix A: One-Dimensional Box Model of Suspended Load Transport

This appendix presents the details of the approach and solution of the system of linear equations for the estimation of suspended masses per estuary stretch under equilibrium conditions. Starting point is equation (6), reproduced here:

$$\frac{\partial}{\partial t}\iiint_{V_i} c dV + \int\int_{S_i} \Phi_k n_k dS = 0, \tag{A1}$$

with $\Phi_k = F_k - cw\delta_{k,3}$, $\delta_{\mu,v}$ being Kroneker's delta. This equation represents the tidally averaged balance of SPM in each stretch and it is obtained by segmenting the estuary in $N = 6$ stretches, each of them defined by the interval (x_i, x_{i+1}), and integrating into the box V_i, defined by the surface S_i.

The following conditions are imposed on the net fluxes, that is, $\Phi_k n_k = 0$ on the banks and the surface, $\Phi_k n_k = F_k$ in the cross section localized at x_i and $\Phi_k n_k = -(E-D)$ in the bed. The latter term represents the balance between erosion, E, and deposition, D. With these conditions, equation (A1) can be expressed as

$$\frac{\partial m_i}{\partial t} + \int\int_{A_{i+1}} F_x dA - \int\int_{A_i} F_x dA - \int\int_{\mathfrak{A}_i} (E-D) dA = 0, \quad i = 1, 2, \ldots, N, \tag{A2}$$

where m_i is the mass kept in suspension in each stretch, A_i the area of the section transversal to the main channel at x_i, and $\mathfrak{A}_i$ the area at the bottom of the control volume V_i.

Assuming (local) morphodynamic equilibrium, i.e., $E-D=0$, and the equilibrium masses, $\widehat{m}_i$, verify $\partial \widehat{m}_i / \partial t = 0$, equation (A2) reduces to

$$\int\int_{A_{i+1}} \widehat{F}_x dA = \int\int_{A_i} \widehat{F}_x dA \quad \text{for } i = 1, \ldots, N. \tag{A3}$$

The symbol $\widehat{\cdot}$ above the variables denotes here its equilibrium value. The fluxes are determined as a decomposition of an advective term plus another diffusive one, $\widehat{F}_x = \widehat{F}_x^{(adv)} + \widehat{F}_x^{(dif)}$. Assuming laterally homogeneous stretches, the advective transport takes the form

$$\int\int_{A_i} \widehat{F}_x^{(adv)} dA = b_i \int_{-\bar{h}_i}^{0} \widehat{F}_x^{(adv)} dz = \left(\widehat{bT}\right)_i, \tag{A4}$$

where b is the channel width and T is the suspended load transport per unit width, both evaluated at each stretch i. The diffusive transport is obtained by approximating the corresponding term by means of simple centered finite differences, giving

$$\int\int_{A_i} \widehat{F}_x^{(dif)} dA \approx -\frac{2K_{h,i}}{\Delta_{i-1}^{i+1}} \left(\frac{\widehat{m}_i}{\Delta_i^{i+1}} - \frac{\widehat{m}_{i-1}}{\Delta_{i-1}^{i}} \right), \tag{A5}$$

with $\Delta_v^\mu \equiv x_\mu - x_v$, and no summation convention. The set of equations defined by equations (A3)–(A5) is completed with the flux in the upstream boundary $\left(\left(\widehat{bT}\right)_{N+1}\right)$ and with the constraint over the partial masses

$$\sum_{i=1}^{N} \widehat{m}_i = M. \tag{A6}$$

In the latter expression, M is the total suspended mass present in the estuary in each tidal cycle. This relationship implies that it is only necessary to propose the set of equation (A3) for $i = 2, \ldots, N$ and, also, it avoids the specification of the transport in the estuary mouth.

Regarding the upstream boundary, the simplest choice for $\left(\widehat{bT}\right)_{N+1}$ is the vanishing-flux condition at the dam of Alcalá del Río. However, no information on transport is available between 57.6 and 110 km. A stretch defined between these two points would have an excessive length (52.4 km), with heterogeneous morphological characteristics. For that reason, the flux is specified at 57.6 km and not at the dam. This

increased the reliability of the computations but reducing the spatial range to the low and central stretches of the estuary. A total of $N = 6$ stretches defined by $x_1 = 0\text{km}, x_2 = 17.3\text{km}, x_3 = 23.6\text{km}, x_4 = 26.2\text{km}, x_5 = 35.3\text{km}, x_6 = 47.1\text{km}$, and $x_7 = 57.6\text{km}$ are therefore considered. These are precisely the ones corresponding to the positions γ_i of the CTDs. At points x_i, with $i = 2, \ldots, N$, the transports are prescribed and, for sake of simplicity, at x_7 a vanishing diffusive flux is assumed.

Applying thus the equations (A4) and (A5) to equation (A3) in these stretches is obtained:

$$\left(\widehat{bT}\right)_i - \frac{2K_{h,i}}{\Delta_{i-1}^{i+1}}\left[\frac{\widehat{m}_i}{\Delta_i^{i+1}} - \frac{\widehat{m}_{i-1}}{\Delta_{i-1}^{i}}\right] = \left(\widehat{bT}\right)_{i+1} - \frac{2K_{h,i+1}}{\Delta_i^{i+2}}\left[\frac{\widehat{m}_{i+1}}{\Delta_{i+1}^{i+2}} - \frac{\widehat{m}_i}{\Delta_i^{i+1}}\right], \tag{A7}$$

for $i = 2, \ldots, N-1$ and

$$\widehat{b}_N\widehat{T}_N - \frac{2K_{h,N}}{\Delta_{N-1}^{N+1}}\left[\frac{\widehat{m}_N}{\Delta_N^{N+1}} - \frac{\widehat{m}_{N-1}}{\Delta_{N-1}^{N}}\right] = \widehat{b}_{N+1}\widehat{T}_{N+1}, \tag{A8}$$

for $i = N$. The set of equations equations (A7) and (A8) is completed by equation (A6) to leave a system of N linear equations with N unknowns $\{\widehat{m}_i\}_{i=1}^N$. The variables of the above set of equations are nondimensionalized with $b_{\text{ref}} = 400$ m, $K_{\text{ref}} = 1.5\times10^3$ m^2/s, $M_{\text{ref}} = 10^8$ kg, $L_{\text{ref}} = 110$ km, and $T_{\text{ref}} = 2K_{\text{ref}}M_{\text{ref}}/\left(b_{\text{ref}}L_{\text{ref}}^2\right) = 0.0620$ kg/m/s. These numbers represent typical values for width, dispersion coefficient, mass, estuary length, and transport, respectively. With this scaling, the resulting system is

$$\mathbf{G}\cdot\mathbf{y} = \mathbf{B}, \tag{A9}$$

where $\mathbf{B}$ is the column vector

$$\mathbf{B} = (M, b_3T_3 - b_2T_2, \ldots, b_{N+1}T_{N+1} - b_NT_N)^t, \tag{A10}$$

and $\mathbf{G}$ is the matrix $N \times N$ constructed from combining equations (A6)–(A8). Its elements $G_{j,i}$ take the form

$$G_{j,i} = \begin{cases} 1 & \text{if } j = 1 \\ \dfrac{K_{h,i}}{\Delta_{i-1}^{i+1}\Delta_{i-1}^{i}} & \text{if } 1 \le j-1 = i \le N \\ -\dfrac{K_{h,i}}{\Delta_{i-1}^{i+1}\Delta_i^{i+1}} - \dfrac{K_{h,i+1}}{\Delta_i^{i+2}\Delta_i^{i+1}} & \text{if } 2 \le j = i \le N \\ \dfrac{K_{h,i+1}}{\Delta_i^{i+2}\Delta_{i+1}^{i+2}} & \text{if } 3 \le j+1 = i \le N \end{cases}. \tag{A11}$$

Finally, $\mathbf{y}$ is a column vector $N\times1$ which contain the unknowns $\widehat{m}_i$

$$\mathbf{y} = (\widehat{m}_1, \widehat{m}_2, \ldots, \widehat{m}_{N+1})^t, \tag{A12}$$

Acknowledgments

This research was funded by the Spanish Ministry of Science and Innovation (project CTM2009-10520/MAR) and by the Department of Innovation, Science and Business of the Andalusian Regional Government (projects P09-TEP-4630 and P09-RNM-4735), and a research contract between the University of Granada, the University of Córdoba, and the CSIC. The data analyzed in this work can be obtained from the authors. The authors are indebted to the two anonymous reviewers for their help in improving this paper. The authors also wish to thank Javier Ruiz and Gabriel Navarro for useful discussions.

References

Amos, C. L., and K. T. Tee (1989), Suspended sediment transport processes in Cumberland Basin, Bay of Fundy, *J. Geophys. Res.*, *94*, 14,407–14,417.

Becker, M. L., R. A. Luettich Jr., and H. Seim (2009), Effects of intratidal and tidal range variability on circulation and salinity structure in the Cape Fear River Estuary, North Carolina, *J. Geophys. Res.*, *114*, C04006, doi:10.1029/2008JC004972.

Blanton, J. O., H. Seim, C. Alexander, J. Amft, and G. Kineke (2003), Transport of salt and suspended sediments in a curving channel of a coastal plain estuary: Satilla River, GA, *Estuarine Coastal Shelf Sci.*, *57*, 993–1006.

Caballero, I., E. P. Morris, J. Ruiz, and G. Navarro (2014), Assessment of suspended solids in the Guadalquivir estuary using new DEIMOS-1 medium spatial resolution imagery, *Remote Sens. Environ.*, *146*, 148–158.

Chernetsky, A. S., H. M. Schuttelaars, and S. A. Talke (2010), The effect of tidal asymmetry and temporal settling lag on sediment trapping in tidal estuaries, *Ocean Dyn.*, *60*, 1219–1241.

Cloern, J. E. (1987), Turbidity as a control on phytoplankton biomass and productivity in estuaries, *Cont. Shelf Res.*, *7*, 1367–1381.

Contreras, E., and M. Polo (2012), Measurement frequency and sampling spatial domains required to characterize turbidity and salinity events in the Guadalquivir estuary (Spain), *Nat. Hazards Earth Syst. Sci.*, *12*(8), 2581–2589.

de Jonge, V. N. (1983), Relations between annual dredging activities, suspended matter concentrations, and the development of the tidal regime in the Ems estuary, *Can. J. Fish. Aquat. Sci.*, *40*, s289–s300.

de Jonge, V. N., H. M. Schuttelaars, J. E. E. van Beusekom, S. A. Talke, and H. E. de Swart (2014), The influence of channel deepening on estuarine turbidity levels and dynamics, as exemplified by the Ems estuary, *Estuarine Coastal Shelf Sci.*, *139*, 46–59.

Díez-Minguito, M., A. Baquerizo, M. Ortega-Sánchez, G. Navarro, and M. Losada (2012), Tide transformation in the Guadalquivir estuary (SW Spain) and process-based zonation, *J. Geophys. Res.*, *117*, C03019, doi:10.1029/2011JC007344.

Díez-Minguito, M., E. Contreras, M. Polo, and M. Losada (2013), Spatio-temporal distribution, along-channel transport, and post-riverflood recovery of salinity in the Guadalquivir estuary (SW Spain), *J. Geophys. Res. Oceans*, *118*, 2267–2278, doi:10.1002/jgrc.20172.

Dyer, K. R. (1995), Sediment transport processes in estuaries, *Dev. Sedimentol.*, *53*, 423–449.

Dyer, K. R. (1997), *Estuaries: A Physical Introduction*, 2nd ed., John Wiley, Chichester, U. K.

Eisma, D. (1993), *Suspended Matter in the Aquatic Environment*, vol. 315, Springer, Berlin Heidelberg.

Friedrichs, C. T., B. D. Armbrust, and H. E. de Swart (1998), Hydrodynamics and equilibrium sediment dynamics of shallow, funnel-shaped tidal estuaries, in *Physics of Estuaries and Coastal Seas*, edited by J. Dronkers and M. Schaffers, pp. 315–327, A. A. Balkema, Brookfield, Vt.

Hagy, J. D., III, and M. C. Murrell (2007), Susceptibility of a northern Gulf of Mexico estuary to hypoxia: An analysis using box models, *Estuarine Coastal Shelf Sci.*, *74*, 239–253.

Hansen, D. V., and M. Rattray (1966), New dimensions in estuary classification, *Limnol. Oceanogr.*, *11*, 319–326.

Hickey, B. M., et al. (2010), River influences on shelf ecosystems: Introduction and synthesis, *J. Geophys. Res.*, *115*, C00B17, doi:10.1029/2009JC005452.

Jay, D. A., and J. D. Smith (1990), Residual circulation in shallow estuaries. 2: Weakly stratified and partially mixed, narrow estuaries, *J. Geophys. Res.*, *95*, 733–748.

Jay, D. A., and J. D. Musiak (1994), Particle trapping in estuarine tidal flows, *J. Geophys. Res.*, *99*, 20,445–20,461.

Jilan, S., and W. Kangshan (1986), The suspended sediment balance in Changjiang estuary, *Estuarine Coastal Shelf Sci.*, *23*, 81–98.

Johnston, S. A., Jr. (1981), Estuarine dredge and fill activities: A review of impacts, *Environ. Manage.*, *5*, 427–440.

Kappenberg, J., and I. Grabemann (2001), Variability of the mixing zones and estuarine turbidity maxima in the Elbe and Weser estuaries, *Estuaries*, *24*, 699–706.

Li, L., X. H. Wang, F. Andutta, and D. Williams (2014), Effects of mangroves and tidal flats on suspended-sediment dynamics: Observational and numerical study of Darwin Harbour, Australia, *J. Geophys. Res. Oceans*, *119*, doi:10.1002/2014JC009987, in press.

Lin, J., and A. Y. Kuo (2001), Secondary turbidity maximum in a partially mixed microtidal estuary, *Estuaries*, *24*, 707–720.

Losada, M., and J. Ruiz (2010), Propuesta metodológica para diagnosticar y pronosticar las consecuencias de las actuaciones humanas en el estuario del Guadalquivir [in Spanish], Tech. Rep. U2C11, Inst. of Mar. Sci. of Andalucía (CSIC), Univ. of Córdoba, Granada, Spain.

Navarro, G., F. J. Gutierrez, M. Díez-Minguito, M. A. Losada, and J. Ruiz (2011), Temporal and spatial variability in the Guadalquivir Estuary: A challenge for real-time telemetry, *Ocean Dyn.*, *61*, 753–765.

Navarro, G., I. Huertas, E. Costas, S. Flecha, M. Díez-Minguito, I. Caballero, V. López-Rodas, L. Prieto, and J. Ruiz (2012), Use of a real-time remote monitoring network (RTRM) to characterize the Guadalquivir estuary (Spain), *Sensors*, *12*, 1398–1421.

Officer, C. B. (1980), Box models revisited, in *Estuarine and Wetland Processes, Mar. Sci. Ser.*, vol. 11, edited by P. Hamilton and K. Macdonald, pp. 65–114, Plenum, N. Y.

Pawlowicz, R., B. Beardsley, and S. Lentz (2002), Classical tidal harmonic analysis including error estimates in MATLAB using T-TIDE, *Comput. Geosci.*, *28*, 929–937.

Postma, H. (1967), Sediment transport and sedimentation in the estuarine environment, *Estuaries*, *83*, 158–179.

Pritchard, D. W. (1969), Dispersion and flushing of pollutants in estuaries, *J. Hydraul. Div. Am. Soc. Civ. Eng.*, *95*, 115–124.

Ruiz, J., M. Polo, M. Díez-Minguito, G. Navarro, E. Morris, E. Huertas, I. Caballero, E. Contreras, and M. Losada (2014), The Guadalquivir estuary: A hot spot for environmental and human conflicts, in Environmental Management and Governance, Coastal Res. Lib., vol. 8, edited by C. W. Finkl and C. Makowski, pp. 199–232, Springer, Heidelberg.

Sanford, L. P., and J. P. Halka (1993), Assessing the paradigm of mutually exclusive erosion and deposition of mud, with examples from upper Chesapeake Bay, *Mar. Geol.*, *114*, 37–57.

Sanford, L. P., and J. P. Y. Maa (2001), A unified erosion formulation for fine sediments, *Mar. Geol.*, *179*, 9–23.

Scully, M. E., and C. T. Friedrichs (2007), Sediment pumping by tidal asymmetry in a partially mixed estuary, *J. Geophys. Res.*, *112*, C07028, doi:10.1029/2006JC003784.

Son, M., and T. J. Hsu (2011), The effects of flocculation and bed erodibility on modeling cohesive sediment resuspension, *J. Geophys. Res.*, *116*, C03021, doi:10.1029/2010JC006352.

Talke, S. A., H. E. de Swart, and V. N. de Jonge (2009a), An idealized model and systematic process study of oxygen depletion in highly turbid estuaries, *Estuaries Coasts*, *32*, 602–620.

Talke, S. A., H. E. de Swart, and H. M. Schuttelaars (2009b), Feedback between residual circulations and sediment distribution in highly turbid estuaries: An analytical model, *Cont. Shelf Res.*, *29*, 119–135.

Traykovski, P., R. Geyer, and C. Sommerfield (2004), Rapid sediment deposition and fine-scale strata formation in the Hudson estuary, *J. Geophys. Res.*, *109*, F02004, doi:10.1029/2003JF000096.

Uncles, R. J. (2002), Estuarine physical processes research: Some recent studies and progress, *Estuarine Coastal Shelf Sci.*, *55*, 829–856.

Uncles, R. J., R. C. A. Elliot, and S. A. Weston (1985), Observed fluxes of water, salt and suspended sediment in a partly mixed estuary, *Estuarine Coastal Shelf Sci.*, *20*, 147–167.

Wai, O. W. H., C. H. Wang, Y. S. Li, and X. D. Li (2004), The formation mechanisms of turbidity maximum in the Pearl river estuary, *Mar. Pollut. Bull.*, *48*, 441–448.

Winterwerp, J. C., and W. G. M. Van Kesteren (2004), *Introduction to the Physics of Cohesive Sediment Dynamics in the Marine Environment*, vol. 56, Elsevier Sci., Amsterdam.

Erratum

In the originally published version of this article, equation (3) was incorrectly typeset. The equation has since been corrected and this version may be considered the authoritative version of record.